Origin of the Size-Dependent Stokes Shift in $CsPbBr_3$ Perovskite Nanocrystals

Michael C. Brennan,[†] John E. Herr,[†] Triet S. Nguyen-Beck,[†] Jessica Zinna,[†] Sergei Rouvimov,[‡] John Parkhill*,[†] and Masaru Kuno*,[†]

†*Department of Chemistry and Biochemistry, University of Notre Dame 251 Nieuwland Science Hall, Notre Dame, Indiana 46556, USA*

‡*Notre Dame Integrated Imaging Facility, University of Notre Dame, Notre Dame, Indiana 46556, USA*

E-mail: mkuno@nd.edu,john.parkhill@nd.edu

Abstract

We report and explain for the first time the existence of a size-dependent Stokes shift in $CsPbBr_3$ nanocrystals (NCs). Stokes shifts range from 115 to 17 meV for NCs with effective edge lengths varying from ∼3 to 13 nm. We show that the Stokes shift is intrinsic to the NC electronic structure and does not arise from extrinsic effects such as residual ensemble size distributions, impurities or solvent-dependent effects. Furthermore, detailed high-resolution transmission electron microscopy focal-series analyses indicate that subdomains of orthorhombic distortions coexist within the predominately cubic lattice of single NCs. The origin of the Stokes shift is elucidated via first-principles calculations. Corresponding theoretical modeling of the $CsPbBr_3$ NC density of states and band structure reveal the existence of an intrinsic confined hole state 260 to 70 meV above the valence band edge state for NCs with edge lengths from ∼2 to 5 nm. As a result, a size-dependent Stokes shift is predicted and is in quantitative agreement

with the experimental data. Comparison between bulk and NC calculations show that the confined hole state is exclusive to NCs. At a broader level, the distinction between absorbing and emitting states in $CsPbBr_3$ is likely a general feature of other halide perovskite NCs and can be tuned via NC size to enhance applications involving these materials.

Introduction

Hybrid lead halide perovskites have been successfully implemented as effective, low-cost light absorbers in photovoltaic devices.[1] Within the relatively short period of time since their rediscovery,[2,3] light-to-electricity conversion efficiencies have exceeded 20%.[4] This success has stimulated tremendous interest in using hybrid perovskites, such as methylammonium lead iodide ($MAPbI_3$, MA=$CH_3NH_3^+$), for solar cells and for a host of other applications.[5] The remarkable properties of bulk lead halide perovskites have motivated research into harnessing the intrinsic size and compositional control over the optical and electrical response of corresponding nanostructured hybrid perovskites.[6]

Recent breakthroughs in colloidal chemistry now permit $MAPbX_3$, $FAPbX_3$ [FA=$CH(NH_2)_2^+$; X=I^-, Br^-, Cl^-] and their all-inorganic counterparts ($CsPbX_3$) to be made as high quality colloidal nanocrystals (NCs),[7–9] nanowires,[10–12] and nanosheets.[13–16] These nanomaterials are especially attractive materials for next-generation lighting and display technologies due to their high photoluminescence quantum yields (QY$\sim$40-90%), narrow emission linewidths (70-140 meV), and size-/composition-tunable band gaps.[7–9] Despite reports that now exist on their electronic structure,[17–19] much less is known about their underlying photophysics and the nature of the emitting state.

In particular, ubiquitous Stokes shifts exist in hybrid[8,13] and all-inorganic lead halide perovskite nanostructures[7,11,13,16] as well as in their thin-film counterparts.[15,20] For $CsPbBr_3$ NCs, the Stokes shift is size-dependent and ranges from 115 to 17 meV for particles with effective edge lengths (l) between $\sim$3 and 13 nm, respectively. This suggests that a distinction

exists between absorbing and emitting states. Although recent studies have discussed the spectral properties and excited-state dynamics of $CsPbBr_3$ NCs,[21,22] the origin of their size-dependent Stokes shift has yet to be explained.

As a historical note, analogous size-dependent Stokes shifts were seen two decades ago in colloidal CdSe quantum dots (QDs). Stokes shifts there likewise ranged from ∼100 to 10 meV for particle diameters between ∼1 and 5 nm.[23] Corresponding research[24] ultimately explained this Stokes shift, yielding a more in-depth understanding about the electronic structure of CdSe QDs, which today are an important model system.[25] A similar elucidation of the origin of the Stokes shift in $CsPbBr_3$ NCs will improve our understanding about the photophysics of this new system and will ultimately be crucial in promoting their eventual use within applications.

In this study, we demonstrate that a size-dependent Stokes shift exists in $CsPbBr_3$ NCs and establish that it is not caused by extrinsic factors. We rationalize the origin of the shift using detailed theoretical calculations of the size-dependent density of states (DOS) and electronic structure of $CsPbBr_3$ NCs. The computational results reveal the existence of an inherent, size-dependent, confined hole state 260 to 70 meV above the valence band edge state for particles with sizes between ∼2 and 5 nm. We also show that the confined hole state is robust across NC size and crystal phase. We propose that this state is relatively dark in absorption due to its low DOS, but bright in emission. This, in turn, explains the experimentally-observed size-dependent Stokes shift. Furthermore, we show that the emitting state possesses low cesium character, likely providing insight into the photoluminescence properties of analogous nanostructured lead halide perovskites (e.g. $MAPbX_3$).

Results and Discussion

Fourteen $CsPbBr_3$ NC ensembles were synthesized using the technique described by Protesescu et al.[7] The resulting NCs adopt cuboidal morphologies and have surfaces passivated

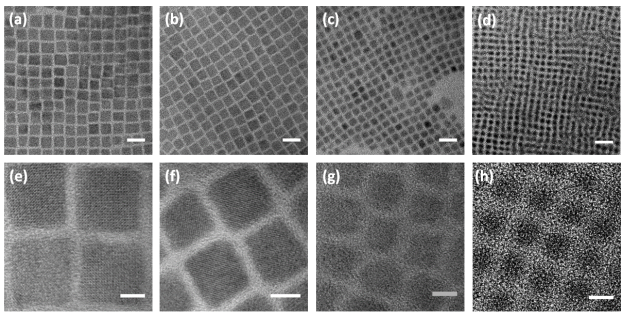

Figure 1: Representative low- [(a) $l = 12.8$ nm, (b) $l = 8.5$ nm, (c) $l = 6.8$ nm, (d) $l = 4.2$ nm] and high- [(e) $l = 12.8$ nm, (f) $l = 8.5$ nm, (g) $l = 6.8$ nm, (h) $l = 4.1$ nm] magnification TEM images of $CsPbBr_3$ NCs. Scale bars on low- and high-magnification images are 20 and 5 nm, respectively.

by oleylammonium and oleate ligands.[26] **Figure 1** shows representative low- and high-magnification TEM images of four ensembles, which span the size series. The low-magnification micrographs show that the NCs form close packed areas with residual size distributions in the range of 5-20%. **Figure S1** shows sizing histograms, which yield effective edge lengths and size distributions. **Figure S2** illustrates an experimental sizing curve extracted from the data. Powder X-ray diffraction (PXRD) patterns shown in **Figure S3** confirm the crystallinity of the NCs.

The electronic structure of lead halide perovskites is known to depend on crystallographic phase.[27] At present, conflicting reports exist in the literature regarding the exact crystal structure adopted by $CsPbBr_3$ nanomaterials. Both cubic[7,16,28] and orthorhombic[29–32] phases have been reported. Most studies utilize ensemble X-ray scattering techniques.[29,32] However, there has yet to be an in-depth study of the atomic structure of $CsPbBr_3$ NCs at the single-particle level.

To investigate the atomic structure of individual $CsPbBr_3$ NCs, we employ a high resolution (HRTEM) focal-series analysis. The technique entails acquiring lattice-resolved HRTEM images of a given NC over progressive defocus values (Δf). By comparing acquired experimental data to simulated images of both orthorhombic and cubic polymorphs, a more definitive structural assignment can be made. However, this technique is particularly challenging for $CsPbBr_3$ NCs due to fast electron-beam induced degradation and random particle orien-

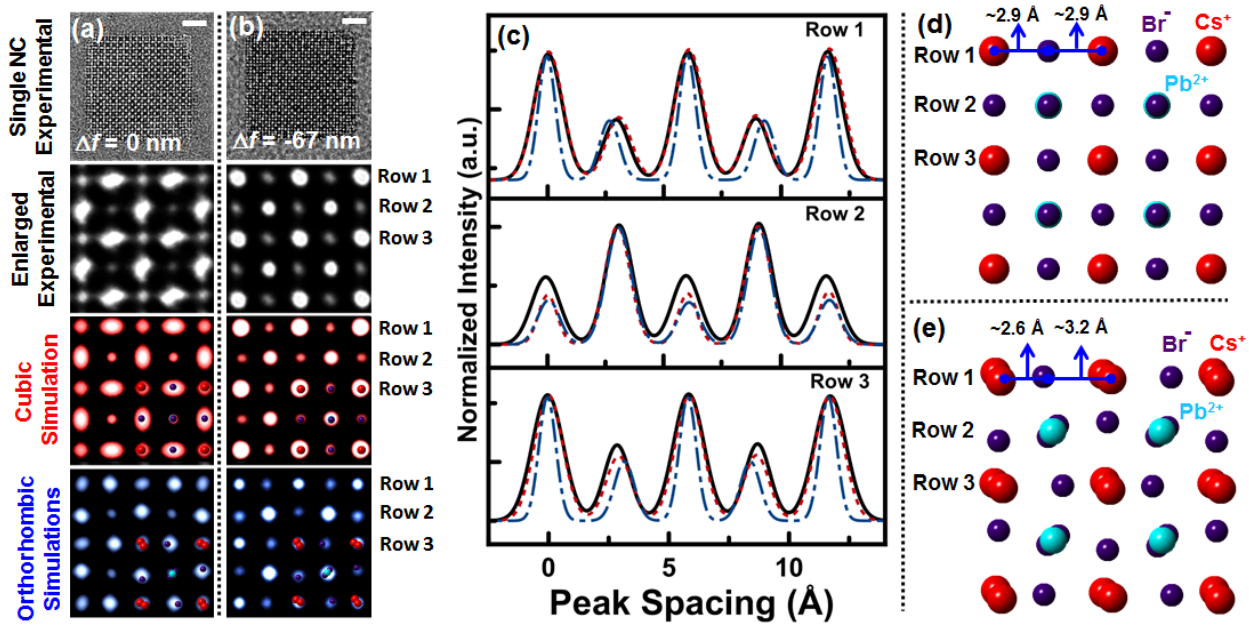

Figure 2: HRTEM focal-series study conducted on an individual $l = 10$ nm NC. HRTEM images acquired at Δf = (a) 0 nm and (b) -67 nm. The top row of images in columns (a) and (b) are the lattice-resolved HRTEM images of an individual NC. Scale bars are 2 nm. Below the single NC images are enlarged areas of the experimental images (black and white) and corresponding simulated cubic (red) and orthorhombic (blue) images. (c) Comparison of the horizontal intensity profiles of the experimental image (solid black), cubic (dashed red), and orthorhombic (dashed-dotted blue) simulations at Δf = -67 nm. Horizontal rows from which the intensity profiles were calculated are the top three atomic rows of each image in (b). (d) Cubic and (e) orthorhombic crystal structure models.

tations.[33,34]

Nonetheless, 12 lattice-resolved HRTEM images were acquired for individual NCs with proper orientation over progressive defocus values taken in 7.5 nm steps. In tandem, fast Fourier transform (FFT) patterns, representative of single NC diffraction patterns, were analyzed as a function of decreasing Δf. **Figure S4** summarizes acquired images and corresponding cubic/orthorhombic simulations.

Figure 2 shows representative experimental HRTEM images of a single $l = 10$ nm NC (top row) as well as enlarged areas (~ 2.25 nm^2) of the NC lattice at $\Delta f = 0$ and -67 nm. Corresponding simulated cubic (red) and orthorhombic (blue) lattice patterns are shown below the experimental data. To quantify the visual comparison, experimental and simulated

intensity profiles along a given row are shown in **Figure 2c** for Δf = -67 nm. The cubic simulation matches well with the experimental data both in terms of relative peak intensities and peak spacing between bright features. Accordingly, the cubic simulation (dashed red lines) in Row 1 shows a uniform peak spacing (d, d = 2.92 Å; **Figure 2d**) in good agreement with experimental values (d = 2.87, 2.96, 2.92, and 2.98 $\mathring{A}$). Conversely, the orthorhombic intensity profile (dashed-dotted blue lines) in Row 1 exhibits alternating peak spacings of d = 2.60, 3.20, 3.20, and 2.60 Å, due to tilting of $PbBr_6$ octahera as depicted in **Figure 2e**. A focal-series analysis performed on a l = 5 nm NC (**Figure S5**) yields similar results. Selected area electron diffraction (SAED) patterns (**Figures S6**) further support assignment of the NC lattice to the cubic phase due to the absence of lower symmetry reflections unique to the orthorhombic phase.

Interestingly, while our focal-series analysis and SAED data suggest that the lattice is predominantly cubic, the FFT analysis across the focal series indicates a coexistence of orthorhombic subdomains.[34] Two of the twelve FFT patterns obtained from l = 10 nm HRTEM images (Δf = -15 and -75 nm, **Figure S7** and **S8**) show unique orthorhombic peaks. At first glance, this observation may stem from electron-beam induced structural changes. However, SAED patterns do not change before and after high magnification electron beam exposure. This suggests that the NC lattice is not altered in the measurement (**Figure S9**). We therefore find the coexistence of small orthorhombic domains within the majority cubic lattice of $CsPbBr_3$, similar to recent reports on atomically thin, two-dimensional $CsPbBr_3$ nanosheets.[34] Further work, including in-line holography with exit wave function reconstruction, is needed to investigate the extent of the orthorhombic distortions within single NCs. Additional information regarding the focal-series study, corresponding cubic/orthorhombic simulations, and complementary FFT/SAED results can be found in the *SI*.

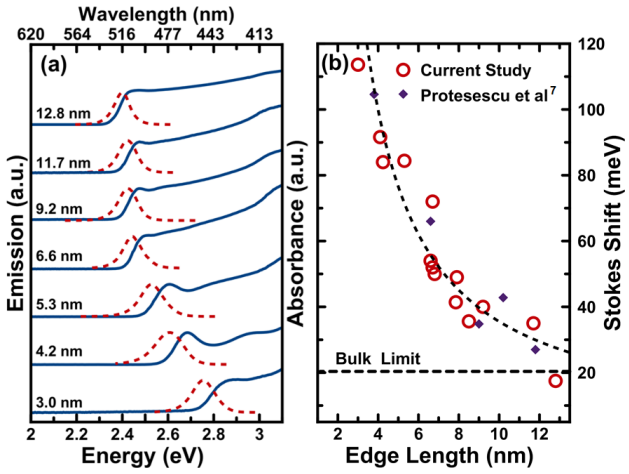

Figure 3: (a) Ensemble absorption (solid blue lines) and emission (dashed red lines) spectra from a small size series of $CsPbBr_3$ NCs dispersed in toluene. Spectra offset for clarity. (b) Size-dependent Stokes shifts from this study and those extracted from the existing literature.[7]

Size-dependent Stokes Shift

We now turn to the linear absorption and emission of $CsPbBr_3$ NCs. **Figure 3a** shows ensemble absorption and emission spectra from seven representative NC ensembles dispersed in toluene. Corresponding edge lengths range from ∼3 to 13 nm. As l decreases, the absorption and emission energy blueshift. This has been explained as stemming from quantum confinement effects given a bulk exciton Bohr radius of $a_0 = 3.5$ nm.[7] Apart from the structured absorption, the high quality of the as-produced NCs is evident from measured photoluminescence quantum yields which range from 30 to 60% (**Table S1**).

The most notable observation from **Figure 3a** is the apparent Stokes shift between the band edge absorption and emission. This Stokes shift decreases with increasing edge length as quantified by fitting acquired ensemble absorption/emission data. Representative absorption fits and extracted data are shown in **Figure S10** and **Table S2** of the *SI*. What emerges is a size-dependent Stokes shift that ranges from 115 to 17 meV as the effective edge length decreases from ∼3 to 13 nm. **Figure 3b** summarizes these shifts and contains additional data points extracted from the literature.[7] Note that the bulk Stokes shift is roughly 20 meV[35] as is indicated by the dashed horizontal line in **Figure 3b**.

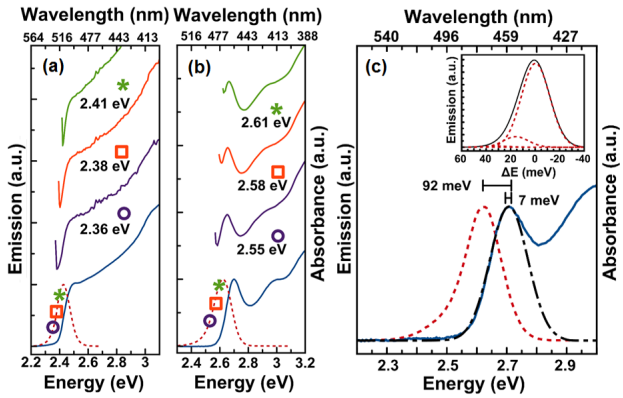

Figure 4: PLE spectra acquired on (a) 8.5 nm and (b) 4.2 nm NC ensembles at three energies on the red edge of their emission spectra. (c) Results of the convolution analysis (dashed-dotted line) for the 4.2 nm ensemble. Associated absorption and emission spectra are shown as solid blue and dashed red lines, respectively. Inset: Modeled single-particle spectrum with a Huang-Rhys parameter of $S = 0.11$.

Room-temperature photoluminescence excitation (PLE) measurements confirm the size-dependent Stokes shift. Namely, **Figures 4a,b** show representative spectra for 8.5 nm (**Figure 4a**) and 4.2 nm (**Figure 4b**) NC ensembles. In each case, PLE spectra were acquired by monitoring the red edge of each sample's band edge emission. Monitored energies are denoted with colored symbols. Resulting PLE spectra match corresponding linear absorption spectra. This correlation is especially evident in the 4.2 nm ensemble where the room-temperature band edge excitonic feature is clearly resolved. To further verify the existence of a Stokes shift, we eliminate other possible extrinsic origins.

First, we examine the time evolution of the emission maximum through time-correlated single photon counting time-resolved emission spectroscopy (TCSPC-TRES). Measurements were performed on $l = 4.1$ and 7.9 nm NC ensembles in toluene. The TCSPC-TRES results shown in **Figure S11** display negligible ($\leq$ 5 meV) redshifting of the emission maximum over the course of 4 ns. The results therefore suggest that solvatochromism or other effects with slow degrees of freedom do not contribute to the apparent Stokes shifts.

To show that the Stokes shift is independent of dielectric media, we have additionally recorded absorption/emission spectra in hexane and chloroform. Resulting Stokes shifts are in quantitative agreement with the data in **Figure 3b** and deviate by no more than 10

meV across solvents. This is illustrated in **Figure S12a**, which plots Stokes shift data from $CsPbBr_3$ ($\epsilon_\infty = 4.96$)[7] NC ensembles dispersed in hexane, toluene, and chloroform (associated static dielectric constants: $\epsilon_{\text{hex}} = 1.88$, $\epsilon_{\text{tol}} = 2.38$, and $\epsilon_{\text{chlo}} = 4.81$).[36] The only observed solvent-dependent effect is a blueshift of absorption/emission spectra in toluene and chloroform relative to that in hexane. This is summarized in **Figure S12b**, which shows absorption/emission spectra of a $l = 4.2$ nm ensemble in the same three solvents. The effect likely stems from dielectric contrast wherein increasing (decreasing) the dielectric contrast between NCs and their surroudning media increases (decreases) exciton binding energies and results in corresponding spectral redshifts (blueshifts).[37]

Finally, we establish that the observed Stokes shift does not originate from the 5-20% residual size distributions of NC ensembles. This is done by convoluting a model single-particle emission spectrum with a Gaussian function, which represents the residual size distribution (∼90-140 meV linewidth established through fits to the linear absorption). The single-particle spectrum is constructed as a phonon progression using a literature longitudinal optical (LO) phonon energy of $\omega_{LO} = 16$ meV[38–40] and a Huang-Rhys parameter (S) that takes values between $S = 0.11$[39] and $S = 0.45$.[40] The inset in **Figure 4b** illustrates the employed single-particle spectrum.

The resulting modeled emission (dashed-dotted line) is plotted relative to the experimental absorption and emission spectrum in **Figure 4c**. The apparent Stokes shift of 7 meV from the modeled emission spectrum differs significantly from the experimentally-determined value of 92 meV. Analogous results have been obtained for 5.3 nm and 11.7 nm ensembles (**Figure S13**). In all cases, modeled Stokes shifts are less than 10 meV. We therefore conclude that residual size distributions of NC ensembles do not account for the observed Stokes shift.

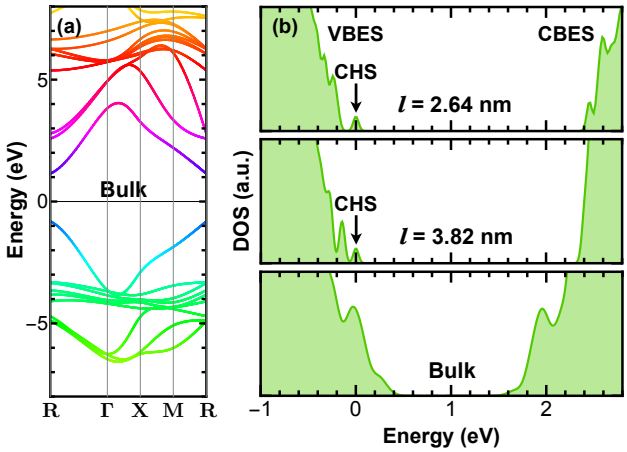

Figure 5: (a) Electronic band structure of $CsPbBr_3$ in the cubic phase calculated with the spin-orbit coupling interaction, and (b) DOS for two NC sizes and the bulk material. The CHS shifts towards the VB edge as the NC size increases, eventually becoming indistinguishable from the bulk VB edge.

Theoretical Models

Having evidenced that the size-dependent Stokes shift in $CsPbBr_3$ NCs cannot be explained by extrinsic factors, we now focus on rationalizing an intrinsic origin by employing first-principles calculations. This requires a description of the electronic structure of bulk $CsPbBr_3$. **Figures 5a,b** show the calculated band structure and projected DOS of bulk cubic $CsPbBr_3$. The band gap occurs at the R point $[k = (1/2, 1/2, 1/2)]$ with an estimated gap energy of 2.16 eV. This agrees well with prior work suggesting a gap energy of 2.39 eV.[41,42] The conduction band (CB) edge is largely Pb p-character whereas the valence band (VB) edge predominately arises from the overlap of Br p -orbitals. Dangling Br (Pb) bonds lead to defect states below (above) the VB maximum (CB minimum). In this regard, bulk $CsPbBr_3$ possesses a surface defect-tolerant electronic structure similar to other lead-based semiconductors (e.g. PbSe).[43] Furthermore, the bulk Stokes shift (20 meV)[35] primarily stems from lattice-induced carrier stabilization and is distinct from the size-dependent shift seen in NCs. Details of bulk $CsPbBr_3$ calculations can be found in the *SI* and **Table S3**.

The size-dependent electronic structure of $CsPbBr_3$ NCs remains relatively unexplored.[19] Our subsequent modeling efforts are premised on the idea that many geometrical

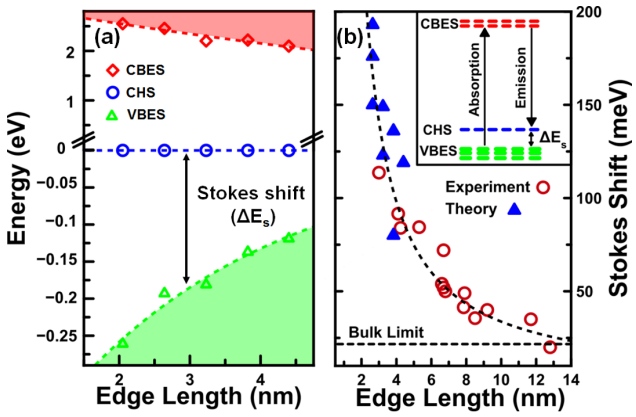

Figure 6: (a) Electronic state energies in $CsPbBr_3$ perovskite NCs of various sizes. State energies are calculated at the Γ-point; dashed lines are the corresponding interpolation fits. The CHS energy level is set to zero. (b) Experimental and theoretical size dependence of the Stoke shift in $CsPbBr_3$ NCs. Inset: model Jablonski diagram.

models must be examined to consider the results robust. Consequently, NC models with edge lengths of l = 2.05, 2.64, 3.23, 3.82, and 4.40 nm were sampled across different morphologies and defects as summarized in **Table S4**. We invoke an adiabatic assumption and that the electron-hole polaronic lattice relaxation is size-independent.[14,44] Calculated (upper limit) exciton binding energies are generally small and range from 30-60 meV. This corroborates a picture wherein diffuse electron-hole pairs weakly interact with the nuclear lattice such that lattice relaxation does not explain the observed size-dependent Stokes shift. Details of these calculations and a further discussion of $CsPbBr_3$ NC exciton binding energies can be found in the *SI*.

All our electronic structure calculations show that the VB frontier state of NCs possesses a spherical spatial distribution delocalized over the entire particle; herein, referred to as the confined hole state (CHS). These calculations use hybrid exchange functionals to suppress the common over-delocalization artifacts of GGAs. The CHS is intrinsic to NCs and qualitatively differs from corresponding bulk VB edge states. Due to its delocalization over the entire NC, this state is confined by the nanocrystal size, providing a means for rationalizing size-dependent Stokes Shifts. Similar electronic structure has been observed in prior theoretical work conducted on $CsPbBr_3$ NCs, further supporting existence of the

CHS.[19] The next occupied NC level (260-70 meV below the CHS) closely resembles the bulk VB maximum at the R point; hereafter referred to as the VB edge state (VBES). **Figure 5** illustrates the CHS relative to the VBES and associated CB edge state (CBES) levels for NCs and the bulk. A projected DOS for a $l = 2.64$ NC model can be found in **Figure S14**.

In our model, NC band edge absorption primarily occurs as a VBES→CBES transition. Subsequent emission occurs after non-radiative relaxation of the hole to the CHS. Consequently, a Stokes shift (ΔE_s) is predicted with a magnitude that is size-dependent, as discussed below. In support of this origin for the Stokes shift, the ratio of calculated VBES→CBES and CHS→CBES absorption strengths are substantial and differ 10- to 50-fold. This originates from differences in their underlying DOS as suggested in **Figure 5**. As a result, the CHS→CBES transition is predicted to be relatively dark in absorption whereas the VBES→CBES transition is bright. The generally small energetic separation of the CHS from the VBES along with significant line broadening of the VBES→CBES transition, stemming from residual size distributions, is likely the reason why this transition is not seen in the absorption. Further discussion and details of the absorption strength estimates can be found in the *SI*.

Figure 6a illustrates calculated energy differences between CHS and VBES states for NCs with edge lengths between $l = 2.64$ nm and $l = 3.82$ nm. Apparent is an increase of the Stokes shift with decreasing edge length, wherein, the size-dependence results from the spatial distribution of the CHS relative to the VBES and the difference between the electronic character of the absorbing and emitting states. This is similar to the explanation for the size-dependent Stokes shift in CdSe QDs.[23,24] Remarkably, both existence of the CHS and accompanying Stokes shift are robust with respect to crystal phase, NC size, and defect type throughout the calculations (see **Figure S15, S16** and **Table S4**). Specifically, a size-dependent CHS→VBES energy difference exists in both cubic and orthorhombic models and across different degrees of surface vacancies.

Subsequent comparison of size-dependent experimental and theoretical Stokes shifts are

plotted in **Figure 6b**. The Stokes shift decreases from 260 to 70 meV for models with $l \sim$ 2 to 5 nm, in good quantitative agreement with experimental values of 115 - 80 meV for particles with $l \sim$ 3 to 5 nm. These observations support the above result indicating the existence of distinct absorbing and emitting states in $CsPbBr_3$ NCs. Moreover, we find that the NC CHS, VBES, and CBES states possess minimal cesium orbital character. Consequently, conclusions from the developed $CsPbBr_3$ NC model are likely applicable to other hybrid lead-halide perovskites.

Conclusion

In summary, we present for the first time the existence of a size-dependent Stokes shift in $CsPbBr_3$ NCs, ranging from 115 to 17 meV for particles with effective edge lengths ranging from ∼3 to 13 nm. We provide experimental proof to show that the shift is intrinsic to the NC electronic structure. Using first-principles modeling, we have identified an inherent, size-dependent CHS level above the VBES, with the CHS dark in absorption and bright in emission. Subsequently, computed Stokes shifts from various geometric models quantitatively agree with experimentally-measured values. The study therefore indicates a distinction between absorbing and emitting states in $CsPbBr_3$ NCs and quantitatively rationalizes observed Stokes shifts. At a broader level, since cesium orbitals do not significantly contribute to the CHS, this state is likely a general feature of other perovskite NCs and can be tuned via NC size to influence their response within photovoltaic or light-emitting applications.

Experimental

Synthesis and Purification of $CsPbBr_3$ NCs

Ensemble NC samples were synthesized with average edge lengths ranging from l = 3.0 - 12.8 nm using a hot injection method previously reported by Protesescu et al.[7] Briefly, 0.18 mmol of $PbBr_2$ (99.999% trace metals basis, Sigma-Aldrich) and 5 mL of octadecene (ODE, 90% technical grade, Acros) were placed in a 10 mL three-neck flask and degassed at 120° C for 1 hour. The reaction vessel was back-filled with N_2. Then 1 mL of oleylamine (80-90% C-18 content, Acros) and 1 mL of oleic acid (90% technical grade, Sigma-Aldrich) were injected into it. The temperature was raised to 140-200° C in order to tune the size with higher (lower) temperatures favoring larger (smaller) NCs. Once the temperature stabilized, 1 mL of a Cs-oleate precursor solution (125 mM in ODE, prepared as described below) was injected. The reaction was then immediately quenched with an ice bath. The precipitate was separated by centrifuging the suspension at 7500 rpm for 10 minutes and was subsequently washed with a 4:1 mixture of toluene:acetone. Note that the addition too much acetone strips the surface ligands, causing them to aggregate. NCs were then dispersed in toluene and isolated using further centrifugation at 7500 rpm for 10 minutes. Recovered NCs were stored in toluene for further analysis.

The Cs-oleate precursor was synthesized according to a previous report.[7] Briefly, 2.5 mmol of Cs_2CO_3 (99.9%, Sigma-Aldrich) was placed in a 100 mL three neck flask with 40 mL of ODE and 2.5 mL of oleic acid. The reaction mixture was degassed at 120° C for 1 hour and was then back-filled with N_2 and heated at 150° C for 6-8 hours. Cs-oleate exists as a precipitate at room temperature and must be heated to 100° C in order to dissolve it prior to injection.

Optical Measurements

Absorption Spectroscopy

Ensemble absorption spectra were obtained on a Cary 50 Bio UV-Visible spectrophotometer. Spectra were recorded under ambient condition in a fused silca cuvette using dilute solutions of $CsPbBr_3$ NCs in toluene. Optical densities were less than 0.3 in all cases.

Photoluminescence and Photoluminescence Excitation Spectroscopy

PL and PLE spectra were recorded under identical conditions as absorption spectra using a Jobin Yvon Fluorolog-3. In both PL and PLE measurements, excitation and emission slit widths were set to 2 nm and 1 nm, respectively. The integration time was 0.25 s with 1 nm increments. For PL measurements, the excitation wavelength was 350 nm. In PLE measurements, emission positions were taken on the red edge of each sample's band edge emission. PLE spectra were corrected for wavelength-dependent variations of the lamp intensity.

Photoluminescence Quantum Yield Measurements

PL QY measurements were performed according to a standardized procedure[45] with appropriate organic dyes [coumarin 6 (QY = 78%)[46] and coumarin 102 (QY = 74%)[47] for the green and blue regions of the spectrum respectively] dissolved in ethanol (100%, Sigma-Aldrich). The NC solvent was toluene. Optical densities were below 0.2 for both dye and NC samples.

Time-Correlated Single Photon Counting Time-Resolved Emission Spectroscopy

TCSPC-TRES measurements were obtained with a Horiba Jobin Yvon TCSPC Spectrometer with a NanoLED 371 nm excitation source. Time-resolved PL decays were measured over 120 nm in 2 nm increments. TCSPC-TRES spectra were constructed by taking slices of PL decay series to obtain the spectrum at a given time after photoexcitation. Note that the

instrument response time is approximately 300 ps. Optical densities were below 0.2 in all cases.

Solvatochromism Measurements

Ensemble samples for solvatochromism experiments were dried via vacuum and were re-dispersed in hexanes and chloroform. Absorption and emission spectra were measured as described above.

Powder X-Ray Diffraction Measurements

Powder XRD measurements were acquired with a Bruker D8 Discover diffractometer with a Cu Kα source ($\lambda = 1.5418$ Å) in the Bragg-Brentano geometry. Measurements were recorded from $10 - 60°$ 2θ with a step size of $0.01°$ and an integration time of 4 s per step.

Transmission Electron Microscopy Measurements

TEM images were acquired using both a FEI Titan 80-300 kV microscope with an accelerating voltage of 300 kV and a JEOL 2011 microscope with an accelerating voltage of 200 kV. Samples were prepared by drop casting dilute NC solutions in toluene onto ultrathin amorphous carbon substrates with copper supports (Ladd). All images in the focal-series study were acquired on the FEI Titan under the same imaging conditions with the exception of the defocus values.

TEM Simulations & Image Processing

Experimental TEM images were Fourier-filtered to remove amorphous carbon background so as to improve their signal-to-noise ratios. All peaks and residual streaks were included in masked areas to avoid possible artifacts. Enlarged experimental lattice images (with dimensions of 1.5×1.5 nm) in **Figure 2, S4,** and **S5** are from approximately the same region

of the NC for each respective defocus value. The corresponding cubic and orthorhombic simulations have identical dimensions (1.5×1.5 nm) to ensure meaningful comparisons. All modeling of HRTEM images and electron diffraction patterns were performed using JEMS software. Orthorhombic (Pnma)[38] simulations were of particles in ⟨010⟩ orientations while cubic (Pm-3m; ICSD 97852) simulations were of particles oriented in the ⟨100⟩ crystal directions. Simulated images were calculated using a multislice method over a wide range of thicknesses (t) and Δf. The best match between simulation and experiment occured at t = 10.5 nm (4.7 nm) for the l = 10 nm (l = 5 nm) NC. In the intensity profile analysis, maximum peak intensities for experimental and simulated data were normalized to 1, and the first peaks were aligned at 0 Å for a given atomic row.

Theoretical Modeling

NC models were created starting with a $n \times n \times n$ supercell, where n is an integer representing the number of cubic unit cells. For the cubic structure, the (100), (010), and (001) directions are identical. Each has two unique layers; one with only Cs and Br atoms and another with only Pb and Br atoms. These are referred to as Cs-Br and Pb-Br layers, respectively. Orthorhombic models were cut to supercells identical in stoichiometry to the cubic models, with the only difference being the tilting of lead-bromide octahedra. Only models terminated on all faces by the same layer, either a Cs-Br or a Pb-Br layer were considered. Pure supercells have three faces terminated by a Cs-Br layer and three faces terminated by a Pb-Br layer. To rectify this with our restriction that surface-terminating layers be identical on all faces, each supercell model was extended by adding a Cs-Br (Pb-Br) layer over the Pb-Br (Cs-Br) surface-terminating faces of the supercell. To correctly simulate these NCs, geometrical models-of-interest must possess the following features: (1) charge neutrality, with near zero dipole moment and a stoichiometry which closely follows the bulk molecular formula, (2) a crystalline structure observed in experiments, and (3) surface defects known to this material. The first requirement puts limitations on the surface-terminating layers

for different-sized models unless defects deeper than the surface layer are considered. For $n \times n \times n$ supercell models, an even integer n requires that the surface be terminated with a Pb-Br layer. An odd integer n requires surfaces to be terminated with a Cs-Br layer. Minimal surface vacancy defects were made to charge neutralize the models while maintaining a near zero dipole. Additional surface vacancy defects were considered to examine their effect on electronic structure as well. $CsPbBr_3$ NCs have high surface defect tolerance, thus defects that break this high tolerance have large formation energies.[18] To validate that this defect tolerance fits with the Stokes shift model posited in the study, a range of surface vacancy defects was explored. Models therefore considered varied placement as well as amount of Cs, Pb, and Br surface vacancies.

Given the debate as to whether $CsPbBr_3$ NCs adopt cubic or orthorhombic phases, models of both phases were prepared. We explore models with two types of optimization: (1) only allowing surface atoms to relax, leaving the core atoms frozen, and (2) allowing to undergo full geometry optimization. Doing so enabled us to rationalize whether there could be characteristics of either morphology or unique NC aspects which explained the Stokes shift.

NC calculations were done in CP2K 4.1[48] with the Heyd-Scuseria-Ernzerhof (HSE) functional,[49] a double-ζ quality basis set[50] and core potentials including relativistic effects.[51] Each model was calculated in a periodic cell with at least 15 Å of vacuum in each direction. Periodic calculations for the bulk cubic and orthorhombic structures were performed in the Quantum Espresso package[52] with the Perdew-Burke-Ernzerhof (PBE0) functional and a 500-eV plane-wave cutoff; scalar relativistic and spin-orbit interactions were included.

Acknowledgments

This work was supported by the Division of Materials Sciences and Engineering, Office of Basic Energy Sciences, U.S. Department of Energy under award DE-SC0014334. J.Z. acknowledges support from the Arthur J. Schmitt Fellowship Foundation. T. S. N.-B. ac-

knowledges the support of the NSF Graduate Research Fellowship under grant DGE-131358 and the Patrick and Jana Eilers Graduate Student Fellowship for Energy Related Research. J. P. thanks the University of Notre Dame's College of Science and Department of Chemistry and Biochemistry, ND Energy and the Honeywell Corporation for generous start-up funding. S. R. thanks the University of Notre Dame Integrated Imaging Facility for financial support of the work conducted on this project.

Author Information Notes

M.C.B and J.E.H. contributed equally to this work.

Associated Content

Supporting Information Available. NC sizing histogram, NC sizing curve, NC PXRD data, TEM defocusing of a $l = 10$ nm NC, TEM defocusing study of a $l = 5$ nm NC, NC SAED data, $l = 10$ nm NC Fourier transformed data across defocus values, $l = 10$ nm NC Fourier transformed comparison of simulation and experiment, SAED before and after electron beam exposure, discussion of FFT and SAED results, table of photoluminescence quantum yields, linear absorption fits, table of relevant experimental absorption and emission data, TCSPC-TRES data, solvatochromism data, convolution analysis of other ensemble NC sizes, discussion of bulk electronic structure calculations, table of calculated bulk band gaps/lattice parameters, discussion of exciton binding energy and absorption strength calculations, table of NC model data, projected DOS for $l = 2.64$ NC model, molecular orbital diagrams for VBES/CHS of different NC sizes, and CHS MOs of NC models with various crystal phases. This material is available free of charge via the Internet at http://pubs.acs.org.

References

(1) Snaith, H. J. *J. Phys. Chem. Lett.* **2013**, *4*, 3623–3630.

(2) Mitzi, D. B.; Feild, C.; Schlesinger, Z.; Laibowitz, R. *J. Solid State Chem.* **1995**, *114*, 159–163.

(3) Kagan, C.; Mitzi, D.; Dimitrakopoulos, C. *Science* **1999**, *286*, 945–947.

(4) National Renewable Energy Labs Efficiency Chart (2017). `https://www.nrel.gov/pv/assets/images/efficiency-chart.png`, (accessed: May 6 2017).

(5) Manser, J. S.; Christians, J. A.; Kamat, P. V. *Chem. Rev.* **2016**, *116*, 12956–13008.

(6) Bai, S.; Yuan, Z.; Gao, F. *J. Mater. Chem. C* **2016**, *4*, 3898–3904.

(7) Protesescu, L.; Yakunin, S.; Bodnarchuk, M. I.; Krieg, F.; Caputo, R.; Hendon, C. H.; Yang, R. X.; Walsh, A.; Kovalenko, M. V. *Nano Lett.* **2015**, *15*, 3692–3696.

(8) Protesescu, L.; Yakunin, S.; Bodnarchuk, M.; Bertolotti, F.; Masciocchi, N.; Guagliardi, A.; Kovalenko, M. *J. Am. Chem. Soc.* **2016**, *10*, 2485–2490.

(9) Zhang, F.; Zhong, H.; Chen, C.; Wu, X.-g.; Hu, X.; Huang, H.; Han, J.; Zou, B.; Dong, Y. *ACS Nano* **2015**, *9*, 4533–4542.

(10) Zhang, D.; Eaton, S.; Yu, Y.; Dou, L.; Yang, P. *J. Am. Chem. Soc.* **2015**, *137*, 9230–9233.

(11) Zhang, D.; Yu, Y.; Bekenstein, Y.; Wong, A. B.; Alivisatos, A. P.; Yang, P. *J. Am. Chem. Soc.* **2016**, *138*, 13155–13158.

(12) Zhu, H.; Fu, Y.; Meng, F.; Wu, X.; Gong, Z.; Ding, Q.; Gustafsson, M. V.; Trinh, M. T.; Jin, S.; Zhu, X.-Y. *Nat. Mater.* **2015**, *14*, 636–642.

(13) Fu, Y.; Meng, F.; Rowley, M.; Thompson, B.; Shearer, M.; Ma, D.; Hamers, R.; Wright, J.; Jin, S. *J. Am. Chem. Soc.* **2015**, *137*, 5810–5818.

(14) Dou, L.; Wong, A. B.; Yu, Y.; Lai, M.; Kornienko, N.; Eaton, S. W.; Fu, A.; Bischak, C. G.; Ma, J.; Ding, T.; Ginsberg, N. S.; Wang, L.-W.; Alivisatos, A. P.; Yang, P. *Science* **2015**, *349*, 1518–1521.

(15) Akkerman, Q. A.; Motti, S. G.; Srimath Kandada, A. R.; Mosconi, E.; D'Innocenzo, V.; Bertoni, G.; Marras, S.; Kamino, B. A.; Miranda, L.; De Angelis, F.; Petrozza, A.; Prato, M.; Manna, L. *J. Am. Chem. Soc.* **2016**, *138*, 1010–1016.

(16) Bekenstein, Y.; Koscher, B. A.; Eaton, S. W.; Yang, P.; Alivisatos, A. P. *J. Am. Chem. Soc.* **2015**, *137*, 16008–16011.

(17) Lang, L.; Yang, J.; Liu, H.; Xiang, H.; Gong, X. *Phys. Lett. A* **2014**, *378*, 290–293.

(18) Kang, J.; Wang, L.-W. *J. Phys. Chem. Lett.* **2017**, *8*, 489–493.

(19) ten Brinck, S.; Infante, I. *ACS Energy Lett.* **2016**, *1*, 1266–1272.

(20) D'Innocenzo, V.; Srimath Kandada, A. R.; De Bastiani, M.; Gandini, M.; Petrozza, A. *J. Am. Chem. Soc.* **2014**, *136*, 17730–17733.

(21) Makarov, N.; Guo, S.; Isaienko, O.; Liu, W.; Robel, I.; Klimov, V. *Nano Lett.* **2016**, *16*, 2349–2362.

(22) Castaeda, J. A.; Nagamine, G.; Yassitepe, E.; Bonato, L. G.; Voznyy, O.; Hoogland, S.; Nogueira, A. F.; Sargent, E. H.; Cruz, C. H. B.; Padilha, L. A. *ACS Nano* **2016**, *10*, 8603–8609.

(23) Efros, A.; Rosen, M.; Kuno, M.; Nirmal, M.; Norris, D.; Bawendi, M. *Phys. Rev. B* **1996**, *54*, 4843–4856.

(24) Kuno, M.; Lee, J.; Dabbousi, B.; Mikulec, F.; Bawendi, M. *J. Chem. Phys.* **1997**, *106*, 9869–9882.

(25) Kuno, M. *J. Phys. Chem. Lett.* **2013**, *4*, 680–680.

(26) Roo, J.; Ibáñez, M.; Geiregat, P.; Nedelcu, G.; Walravens, W.; Maes, J.; Martins, J.; Driessche, I.; Kovalenko, M.; Hens, Z. *ACS Nano* **2016**, *10*, 2071–2081.

(27) Stoumpos, C. C.; Kanatzidis, M. G. *Acc. Chem. Res.* **2015**, *48*, 2791–2802.

(28) Tong, Y.; Bladt, E.; Aygüler, M. F.; Manzi, A.; Milowska, K. Z.; Hintermayr, V. A.; Docampo, P.; Bals, S.; Urban, A. S.; Polavarapu, L.; Feldmann, J. *Angew. Chem. Int. Ed.* **2016**, *55*, 13887–13892.

(29) Cottingham, P.; Brutchey, R. *Chem. Commun.* **2016**, *52*, 5246–5249.

(30) Swarnkar, A.; Chulliyil, R.; Ravi, V. K.; Irfanullah, M.; Chowdhury, A.; Nag, A. *Angew. Chem.* **2015**, *127*, 15644–15648.

(31) Pan, A.; He, B.; Fan, X.; Liu, Z.; Urban, J. J.; Alivisatos, A. P.; He, L.; Liu, Y. *ACS Nano* **2016**, *10*, 7943–7954.

(32) Bertolotti, F.; Protesescu, L.; Kovalenko, M. V.; Yakunin, S.; Cervellino, A.; Billinge, S. J. L.; Terban, M. W.; Pedersen, J. S.; Masciocchi, N.; Guagliardi, A. *ACS Nano* **2017**, *11*, 3819–3831.

(33) Dang, Z.; Shamsi, J.; Palazon, F.; Imran, M.; Akkerman, Q. A.; Park, S.; Bertoni, G.; Prato, M.; Brescia, R.; Manna, L. *ACS Nano* **2017**, *11*, 2124.

(34) Yu, Y.; Zhang, D.; Kisielowski, C.; Dou, L.; Kornienko, N.; Bekenstein, Y.; Wong, A. B.; Alivisatos, A. P.; Yang, P. *Nano Lett.* **2016**, *16*, 7530–7535.

(35) Rakita, Y.; Kedem, N.; Gupta, S.; Sadhanala, A.; Kalchenko, V.; Bhm, M. L.; Kulbak, M.; Friend, R. H.; Cahen, D.; Hodes, G. *Cryst. Growth Des.* **2016**, *16*, 5717–5725.

(36) Lide, D.; Haynes, W. *CRC Handbook of Chemistry and Physics*, 90th ed.; CRC Press: Boca Raton, 2009.

(37) Muljarov, E.; Zhukov, E.; Dneprovskii, V.; Masumoto, Y. *Phys. Rev. B* **2000**, *62*, 7420.

(38) Stoumpos, C. C.; Malliakas, C. D.; Peters, J. A.; Liu, Z.; Sebastian, M.; Im, J.; Chasapis, T. C.; Wibowo, A. C.; Chung, D. Y.; Freeman, A. J.; Wessels, B. W.; Kanatzidis, M. G. *Cryst. Growth Des.* **2013**, *13*, 2722–2727.

(39) Sebastian, M.; Peters, J.; Stoumpos, C.; Im, J.; Kostina, S.; Liu, Z.; Kanatzidis, M.; Freeman, A.; Wessels, B. *Phys. Rev. B* **2015**, *92*, 235210.

(40) Pushuk, I.; Pidzyrajlo, N. S.; Matsko, M. G. *Fiz. Tverd. Tela* **1981**, *23*, 2162–2165.

(41) Begum, R.; Parida, M. R.; Abdelhady, A. L.; Murali, B.; Alyami, N.; Ahmed, G. H.; Hedhili, M. N.; Bakr, O. M.; Mohammed, O. F. *J. Am. Chem. Soc.* **2017**, *139*, 731–737.

(42) Zhang, X.; Lin, H.; Huang, H.; Reckmeier, C.; Zhang, Y.; Choy, W. C.; Rogach, A. L. *Nano Lett.* **2016**, *16*, 1415–1420.

(43) Allan, G.; Delerue, C. *Phys. Rev. B* **2004**, *70*, 245321.

(44) Emin, D. *Phys. Rev. B* **1971**, *4*, 3639.

(45) Grabolle, M.; Spieles, M.; Lesnyak, V.; Gaponik, N.; Eychmller, A.; Resch-Genger, U. *Anal. Chem.* **2009**, *81*, 6285–6294.

(46) Reynolds, G. A.; Drexhage, K. H. *Opt. Commun.* **1975**, *13*, 222–225.

(47) Jones, G.; Jackson, W. R.; Halpern, A. M. *Chem. Phys. Lett.* **1980**, *72*, 391–395.

(48) (a) Bortnik, U.; VandeVondele, J.; Weber, V.; Hutter, J. *Parallel Comput.* **2014**, *40*, 4758; (b) Hutter, J.; Iannuzzi, M.; Schiffmann, F.; VandeVondele, J. *Wiley Interdiscip. Rev. Comput. Mol. Sci.* **2014**, *4*, 15–25; (c) Guidon, M.; Hutter, J.; VandeVondele, J.

J. Chem. Theory Comput. **2010**, *6*, 2348–2364; (d) Guidon, M.; Hutter, J.; VandeVondele, J. *J. Chem. Theory Comput.* **2009**, *5*, 3010–3021; (e) Genovese, L.; Deutsch, T.; Goedecker, S. *J. Chem. Phys.* **2007**, *127*, 054704; (f) Genovese, L.; Deutsch, T.; Neelov, A.; Goedecker, S.; Beylkin, G. *J. Chem. Phys.* **2006**, *125*, 074105; (g) VandeVondele, J.; Krack, M.; Mohamed, F.; Parrinello, M.; Chassaing, T.; Hutter, J. *Comput. Phys. Commun.* **2005**, *167*, 103 – 128; (h) Frigo, M.; Johnson, S. G. *Proc. IEEE* **2005**, *93*, 216–231; (i) VandeVondele, J.; Hutter, J. *J. Chem. Phys.* **2003**, *118*, 4365–4369.

(49) Heyd, J.; Scuseria, G. E. *J. Chem. Phys.* **2004**, *120*, 7274–7280.

(50) VandeVondele, J.; Hutter, J. *J. Chem. Phys.* **2007**, *127*, 114105.

(51) Krack, M. *Theor. Chem. Acc.* **2005**, *114*, 145–152.

(52) Giannozzi, P. et al. *J. Phys. Condens. Matter* **2009**, *21*, 395502.

Graphical TOC Entry

